Journal of Materials Chemistry A

Accepted Manuscript

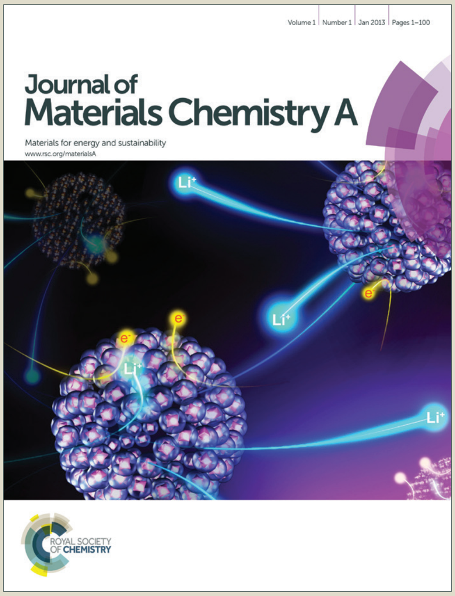

Volume 1 | Number 1 | Jan 2013 | Pages 1–100

Journal of Materials Chemistry A

Materials for energy and sustainability

www.rsc.org/materialsA

ROYAL SOCIETY OF CHEMISTRY

www.rsc.org/materialsA

Synergetic effect of graphene on Cu_2O nanowire arrays as highly efficient hydrogen evolution photocathode in water splitting

Amare Aregahegn Dubale[1], Wei-Nien Su[2,*] Andebet Gedamu Tamirat[1], Chun-Jern Pan[1], Belete Asefa Aragaw[1], Hong-Ming-Chen[1], Ching-Hsiang Chen[2] and Bing-Joe Hwang[1,3*]

[1]NanoElectrochemistry Laboratory, Department of Chemical Engineering, National Taiwan University of Science and Technology, Taipei 106, Taiwan.
[2]NanoElectrochemistry Laboratory, Graduate Institute of Applied Science and Technology, National Taiwan University of Science and Technology, Taipei 106, Taiwan.
[3]National Synchrotron Radiation Research Center, Hsinchu 30076, Taiwan.
*Corresponding authors: bjh@mail.ntust.edu.tw; wsu@mail.ntust.edu.tw

Abstract:

A one dimensional (1D) Cu_2O straddled with graphene is proposed as a highly promising and stable photocathode for solar hydrogen production. The Cu_2O nanowire arrays modified with optimized concentration of graphene provide much higher improved photocurrent density −4.8 mA cm^{-2}, (which is two times that of bare 1D Cu_2O, −2.3 mA cm^{-2}), at 0 V vs RHE under AM 1.5 illumination (100 mW cm^{-2}) and solar conversion efficiency reaching 3.3% at an applied potential of −0.55 V vs Pt counter electrode. Surprisingly, 1D Cu_2O with optimum graphene concentration exhibit inspiring photocurrent density of 2.1 to 1.1 mA cm^{-2} at a higher positive potential range of 0.2−0.4 V vs RHE, which is 300−550% higher compared with bare 1D Cu_2O. This is the highest value ever reported for a Cu_2O-based photocathode at such positive potential. After 20 minute of standard solar irradiation, 83% of the initial photocurrent density retained for the nanocomposite which is more than five times compared to the bare Cu_2O (14.5%). Faradic efficiency of 74% was obtained for the evolved H_2 gas measurement. To get evidence for the photostability of graphene modified photocathode, a detailed characterization was carried out. The high PEC performance of graphene/Cu_2O nanocomposite is attributed to the improved crystallinity and the synergetic effect of graphene in absorbing the visible light, suppressing the charge recombination and photocorrosion of the photoelectrode by preventing direct contact with the electrolyte. This inexpensive photocathode prepared free of noble metals, showed enhanced high photocurrent density with good stability and is a highly promising photocathode for solar hydrogen production.

Keywords: PEC, Cu_2O, nanowire arrays, graphene, photocathode, hydrogen production, water spitting

1. Introduction

Hydrogen production from carbon-free, green energy resources via solar splitting of water into hydrogen[1] has been considered as a promising hydrogen fuel production since its discovery by Honda and Fujishima in 1972.[2] Photoelectrochemical (PEC) cells, which utilize sunlight to directly split water at the semiconductor-electrolyte interface, have attracted a lot of interest in academic research[3] and industry[4] because of the potential of cost-effective production of hydrogen [5] with high efficiency[6] for renewable energy.

Many semiconductors, including TiO_2, CdS, $SrTiO_3$, WO_3, CuO and the likes,[7-11] have been reported having the ability to generate hydrogen. Among them, Cu_2O is considered as a promising and attractive material for solar driven hydrogen production due to having relatively narrow band gap (ca. 2.0 eV), which makes it effective in harvesting visible light,[12] with a sufficiently more negative conduction band provides ease of water reduction reaction within this narrow band gap. The maximum absorption of visible light by its band gap will also provide a theoretical photocurrent of 14.7 $mAcm^{-2}$ and a light-to-hydrogen conversion efficiency of 18% based on the AM 1.5 spectrum.[13] Cuprous oxide is cheap, environmentally benign and can be produced from inexpensive material involving hazardous free manufacturing process. Furthermore, the position of the Fermi level of the cuprous oxide,[14] suggests the possibility of constructing a standalone device for water splitting by coupling it with an n-type semiconductor electrode, such as n-WO_3.[15]

In addition to photocatalyst for solar-driven water splitting and H_2 generation,[16] Cu_2O has been used in various applications, as an electrocatalyst for the O_2[17] or CO_2 reduction,[18] as an anode material for lithium ion batteries[19] and as a p-type semiconductor in fabricating a p-n junction structure for solar cell applications.[20] However, working on Cu_2O as a photocathode material for water reduction reaction involve major problems such as its poor stability in the aqueous solution and shorter electron diffusion length (10–100 nm),[14] than that of the light absorption depth near the band gap (approximately 10 μm).[21] The former problem is because of the oxidation and reduction potential of univalent copper oxide which lies within the band gap resulting competitive reactions during water splitting.[13] Thus, inhibiting self photocorrosion and enhancing the electron diffusion length requires the use of cost effective and potential nano-coating material and preparation of high crystallinity 1D nanostructures respectively.

Carbon nanomaterials like carbon nanodots,[22] graphene,[23, 24] fullerene,[25] and graphene quantum dots (QDs)[26] have attracted tremendous research interest towards application of solar to energy conversion material due to their corrosion resistance, ease of accessibility, and unique surface properties. Graphene, a two dimensional honeycomb structure achieved by the organization of an atomic sheet of sp^2 bonded carbon atoms, has been extensively investigated for its remarkable electrical and mechanical properties.[27] It, being not only the thinnest ever but also the strongest material, has in fact the potential for nano-coating applications. When sticking to or growing on various surfaces, graphene adds only negligible thickness to the size of the underlying sample and forms an electrically and thermally conductive coating on it.[28] Furthermore, graphene is known for its good transparency in both the visible and near-infrared regions, and as a good electron acceptor. When blended with semiconductors, it helps to enhance the charge separation and it is also uniquely suitable for preventing surfaces of metals and semiconductors from oxidation.

Recently, tremendous research reports towards fabrication of graphene based composites containing metal sulfides; metal oxides and metal nanoparticles have been reported for enhancing photocatalytic activities.[29, 30] But still little attention has been concentrated on graphene/Cu_2O nanocomposites. Lately, Phong et al. incorporated graphene with Cu_2O nanoparticles, achieving a maximum photocurrent density of -0.12 mA cm^{-2} at -0.4 V vs Ag/AgCl.[31] Independent studies by Benxia et al.[32], Bo Shen et al.[33] and Niu Zhigang[34] also investigated enhanced photocatalytic performance of Cu_2O nanoparticles immobilized in reduced graphene oxide (Cu_2O/rGO) which resulted in increased photodegradation activity of Rhodamine B, red water and methylene blue as well as efficient charge transportation and separation from Cu_2O to rGO. However, the enhanced photocurrent density and the anti photocorrosion behavior of graphene based Cu_2O nanowire arrays were not investigated in details before. It is therefore necessary to examine the photostabilities of graphene based 1D Cu_2O nanocomposites to enable their use in PEC applications.

Most graphene-based researches focus on the immobilization of nanoparticles on graphene sheets, however, in PEC application, the one-dimensional (1D) nanostructures such as nanowire array or nanotubes are more favored because their unique morphology can offer a direct path for the photogenerated charges, with reduced grain boundaries and high crystallinity, resulting in superior charge transport properties.[35] Owing to the suppressed scattering of free electrons, it is feasible to achieve higher photocatalytic activity of 1D nanomaterial than nanoparticles.[36] However, in the PEC system, it is proved that the direct contact of the Cu_2O photocathode with electrolyte leads to self photocorrosion of Cu_2O. Hence, to prevail this problem combating direct contact of electrode surface with aqueous electrolyte solution requires designing an appropriate and efficient protective layer.

Although there are some reports utilizing inorganic oxides during the synthesis of inorganic oxides–Cu_2O nanocomposite (e.g. $TiO|Al_2O_3/ZnO/Pt$[13], $TiO|Al_2O_3/ZnO/RuO_2$[37]) as a potential protective layer towards inhibiting the photocorrosion and improving the photostability, the costly atomic layer deposition and complex fabrication processes limit their wide application, not to mention the use of expensive Pt or RuO_2 as co-catalysts. In situ protection strategy of Cu_2O with CuO,[38] carbon coating by carbonization of glucose[39] and metal oxide co-catalyst (NiO-$Ni(OH)_2$)[15] with the help of spin coating on pre-synthesized Cu_2O also show enhanced photostability and reduced recombination losses. However, CuO film protection is not suitable for 1–D nanostructure and the mechanism of improved photocurrent density by carbonization of glucose is not yet known. In this study we proposed a facile method to prepare a 1D-nanocomposite electrode of graphene/Cu_2O nanowire arrays (NWAs)/Cu mesh combining electrochemical anodization, dip coating and annealing. The effect of graphene concentration in suppressing photocorrosion problem from the direct contact between Cu_2O NWAs/Cu mesh and electrolyte solution and enhancing photo-response and photostability was investigated.

2 Experimental Procedures

2.1 Preparation of GO

All reagents were of analytical grade and used as obtained without further purification. Graphene oxide (GO) was synthesized from pristine graphite powder (>99.8%, Alfa Aesar) by using a modified Hummers method.[40] Briefly, 3.0 g of graphite powder and 2.0 g of $NaNO_3$ were added into 69 ml of ice cooled conc. H_2SO_4. Then 9.0 g of $KMnO_4$ was gradually added in portion while stirring and cooling continuously to maintain the temperature below 20 ˚C. The reaction was warmed to 35 ˚C and stirred for 30 minutes, at which time water (138 ml) was added slowly, producing a large exotherm to 98 ˚C. External heating was introduced to maintain the reaction temperature at 98 ˚C for 15 minutes, then the heat was removed and the reaction was cooled using a water bath for 10 minutes. The reaction was terminated by adding 420 ml of distilled water followed by 17 ml of 30% H_2O_2 aqueous solution. The resulting mixture was washed with 5% HCl and graphene oxide powder was collected by freeze drying.

2.2 Preparation of Nanostructured $Cu(OH)_2$ on the Copper Mesh Substrate

Pure Cu mesh (100 mesh, 0.11 mm as wire diameter) was purchased from Alfa Aesar. The anodization of a copper mesh substrate in an aqueous solution of NaOH was used to produce the $Cu(OH)_2$ nanostructures on the copper mesh substrate. $Cu(OH)_2$ nanowire arrays (NWAs) were grown in a two-electrode cell with copper mesh as the working electrode and platinum mesh as the counter electrode in 3.0 M aqueous solution of NaOH as electrolyte at ambient conditions.[39, 41] The solution was deaerated by bubbling with dry N_2 for 30 min before experiments. Next, $Cu(OH)_2$ films were electrochemically grown at a constant current density of 10 mA cm^{-2} with a typical reaction time of 1800 s at a temperature of 25 ˚C (cooler controlled). Finally, the copper mesh with the product ($Cu(OH)_2$ NWAs/Cu mesh) was taken out from the solution and washed with distilled water and dried under vacuum at room temperature before characterizations.

2.3 Preparation of x-graphene/Cu_2O nanostructure composite

In a typical synthesis of the graphene/Cu_2O nanostructure composite, different concentration of GO (0, 0.25, 0.50, 0.75, 1.0, 1.5 and 3.0 mg mL^{-1}) was prepared by dispersing GO powder in deionized water upon ultrasonication for 1 hour. Then, the anodized $Cu(OH)_2$ NWAs/Cu mesh was soaked into an aqueous GO dispersion solution for 20 minutes, dried at ambient condition, and then annealed at 500 ˚C in N_2 atmosphere for 4 h to form graphene/Cu_2O NWAs/Cu mesh composite. Finally, the sample was naturally cooled to room temperature. For comparison, graphene and bare Cu_2O NWAs/Cu were prepared by directly reducing GO and $Cu(OH)_2$ NWAs/Cu mesh following the same procedure respectively. For the ease of our discussion, assuming that the conversion of GO to graphene is unity, we designate the graphene film over Cu_2O NWAs/Cu mesh samples with G-x/Cu_2O NWAs/Cu mesh in which x refers the concentration (mg mL^{-1}) of GO and/or graphene solution. For simplicity, the material names $Cu(OH)_2$ NWAs/Cu mesh, Cu_2O NWAs/Cu mesh and G-x/Cu_2O NWAs/Cu mesh were also written as $Cu(OH)_2$/Cu mesh, Cu_2O/Cu mesh and G-x/Cu_2O/Cu mesh respectively.

2.4 Structure Characterization

The electrodes were characterized by XRD, SEM, DRS Uv-Vis, Raman, XPS and XAS. X-ray diffraction (XRD) pattern were acquired with a D2 phaser XRD-300 W, with measurements taken using Cu K_α radiation at 40 kV and 100 mA. Spectra were obtained with a linear silicon strip `Lynx Eye' detector from 20° to 80° at a scan rate of 3° min^{-1}. The morphology of the electrodes were characterized using Field Emission Scanning electron microscopy (EDX JSM 6500F, JEOL). The TEM images were collected on a Philips/FEI Tecnai 20G2 S-Twin apparatus. For TEM analysis, the samples were scratched from the Cu mesh substrate and dispersed ultrasonically in ethanol and applied to a carbon coated copper grid; the solvent was then evaporated in an oven at 80 °C for 6 hours. The diffuse reflectance UV-vis adsorption spectra were obtained using a JASCO (ISV-469) V 560 UV-Vis spectrometer with fine $BaSO_4$ powder as reference. Raman measurements were performed on a ProMaker confocal Raman microscope system as integrated by Protrustech Co., Ltd. A solid state laser operating at λ= 532 nm was used as the excitation source with a laser power of 20 mW to circumvent degradation with 10 s exposure times and 15 accumulations. XPS data were collected using a Thermo VG Scientific Theta Probe with Al K_α target and 1486.6 eV energy at a maximum power of 15 kW. The surface of the sample was cleaned using a 5 kV argon ion gun. The hard X-ray absorption spectra (XAS) were collected at the beam line BL17C1 of National Synchrotron Radiation Research Center (NSRRC) at Hsinchu, Taiwan. The storage ring of the electronic accelerator can supply the electronic energy of 1.5 GeV and the operation current at 360 mA. A Si double crystal monochromator was used to perform energy scan, of which the parallelism can be adjusted to eliminate the high order harmonics. All XAS data were recorded using the fluorescence mode.

2.5 Photoelectrochemical measurement

The photoelectrochemical performance of the electrodes was assessed in a three electrode system using an aqueous solution of 1.0 M Na_2SO_4 buffered at pH 5 with potassium phosphate (0.1 M). The three-electrode configuration consists of Ag/AgCl in saturated KCl as reference electrode, a Pt wire as the counter electrode and the prepared G-x/Cu_2O/Cu mesh as working electrode. The photoresponse of the synthesized electrode was acquired under chopped illumination from a 300 W Xenon lamp equipped with AM 1.5 filter. The intensity of light source was calibrated with a Si diode (Newport) to simulate AM 1.5 illumination (100 mW cm^{-2}). For all the samples, a scan rate of 10 mV s^{-1} was used for the current versus potential measurements (LSV). Photocurrent stability tests were performed by measuring the photocurrent produced under chopped light irradiation (on/off cycles of 10 s) at a fixed biasing potential of 0 V versus RHE. During the PEC tests, the electrolyte was constantly purged with N_2 for 30 minutes. The electrochemical impedance spectroscopy (EIS) was performed using an electrochemical impedance analyser with an AC amplitude of 10 mV and frequency range between 100 kHz to 0.1 Hz. The measured EIS data were obtained at an applied bias of 0 V vs RHE at 25 ˚C. The ABPE (Applied Bias Photon-to-current Efficiency) measurement was performed in two-electrode system (G-1.0/Cu_2O/Cu mesh and Pt as working and counter electrode respectively) using an aqueous solution of 1.0 M Na_2SO_4 buffered at pH 5 with potassium phosphate (0.1 M).under simulated AM 1.5G solar light irradiation (100 $mWcm^{-2}$)

2.6. Photoelectrocatalytic hydrogen measurement

The photocurrent stability test coupled with hydrogen quantification experiments was performed at an applied potential of 0 V vs RHE with visible light illumination that simulate AM 1.5 illuminations (100 mW cm^{-2}) on Cu_2O/Cu mesh and G-1.0/Cu_2O/Cu mesh electrodes for 20 minutes. During the experiment, the evolved hydrogen gas that displaces the water volume was collected above the water through a tube connected to a separate burette equipped with rubber septum as head cap. After driving the PEC reaction (phototstability test) for 20 minutes, the gas was sampled from head cap of the burette with a gas-tight syringe and analyzed by a YANGI–LiN gas chromatograph (column porapax N, Molecular sieve 5A, PDHID detector, with helium carrier gas.). The amount of H_2 produced which is linearly related with peak area given by the PDHID detector was quantified following the calibration curve performed on the GC by introducing known quantities of 5% H_2/Ar. The total charge was obtained from integration of the measured current over time using graphing software OriginPro 8.5.

3 Results and Discussion

Cu mesh is selected as a photocathode material because it is a conductive substrate and can serve as a precursor of Cu_2O nanowire array directly. In addition, the unique open area of the mesh benefits the flow of electrolyte and the mesh structure provides extra lateral surface in comparison to a Cu foil/sheet.[41]

The fabrication process and formation mechanism of graphene/Cu_2O/Cu mesh nanocomposite and Cu_2O/Cu mesh photocathode is illustrated in Scheme 1. The Cu mesh (scheme 1a) is galvanometrically anodized in 3 M NaOH electrolyte solution with 10 mA cm^{-2} at 25 ˚C for 30 minutes, resulting formation of uniform and densely populated blue colored $Cu(OH)_2$ nanowire arrays on the Cu mesh substrate (scheme 1b) which is exactly the same with the natural color of $Cu(OH)_2$ which is blue (digital photograph on scheme 1b). In this work, the Cu_2O/Cu mesh in the presence or absence of graphene was fabricated by a facile and simple thermal reduction process, in which the reduction of both $Cu(OH)_2$ nanowire array and the reduction of GO were achieved in a single step reaction. More typically, the hydrophilic substrates ($Cu(OH_2)$/Cu mesh) was dipped into chemically exfoliated GO sheets (scheme 1c), dried at ambient condition, and then annealed at 500 ˚C in N_2 atmosphere (scheme 1d) to form smooth graphene over Cu_2O/Cu mesh. Likewise, the bare Cu_2O/Cu mesh (scheme 1e) was prepared by direct annealing of the $Cu(OH)_2$/Cu mesh (scheme 1b). Since the key strategy in this work is to investigate synergetic effect of graphene with Cu_2O nanowire array towards PEC performance, different concentrations of GO (0.25, 0.50, 0.75, 1.0, 1.5 and 3.0 mg mL^{-1}) was tested to create graphene over Cu_2O/Cu mesh with efficient PEC performance. As known, surfaces of the chemically exfoliated GO sheets are covered by a large number of epoxy and hydroxyl groups at the basal plan, while carbonyl and carboxyl groups are located at the edges.[42] Thus, taking the advantages of those functional groups on exfoliated GO sheet which act as anchor sites to facilitate the subsequent attachment with hydrophilic part of the $Cu(OH)_2$ via intermolecular hydrogen bonds or coordination bonds,[32] ultimately leads to the formation of Cu-O-C bond. This will be discussed later in Raman section.

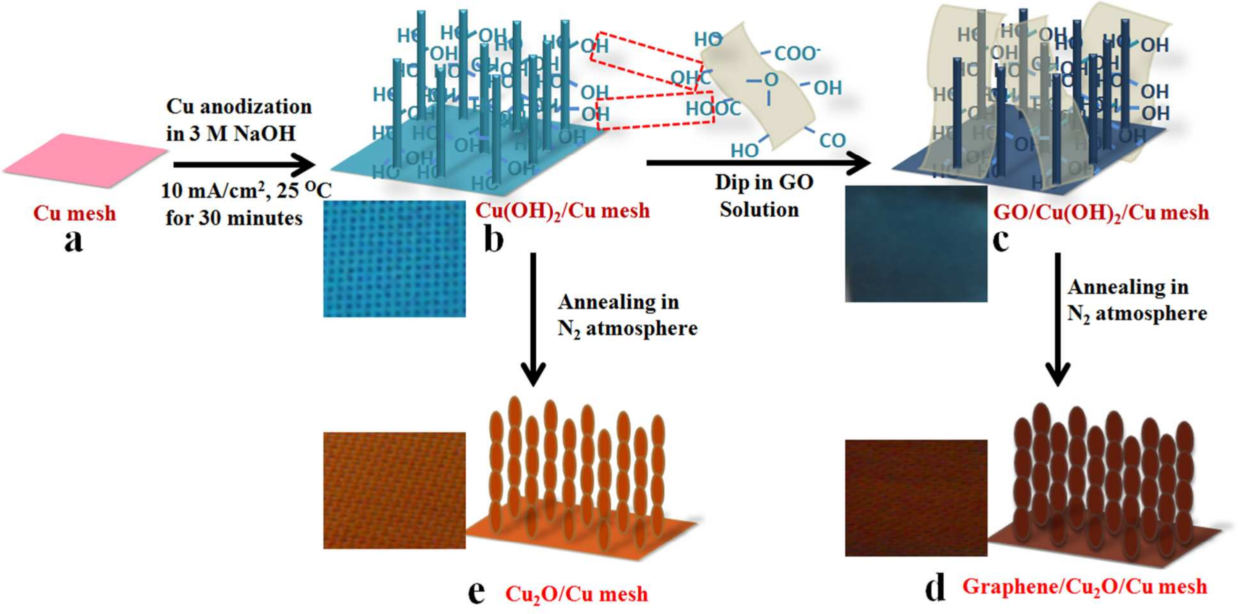

Scheme 1 Synthesis approach of graphene/Cu_2O/Cu mesh and digital photograph in the underneath: (a) electrochemical anodization of Cu mesh in 3.0 M NaOH solution; (b) growing $Cu(OH)_2$ nanowire array on the Cu mesh; (c) formation of GO/$Cu(OH)_2$/Cu mesh composite; (d) thermal reduction of GO/$Cu(OH)_2$/ Cu mesh to graphene/Cu_2O/Cu mesh; (e) reference sample of $Cu(OH)_2$/ Cu mesh reduced to Cu_2O/Cu mesh

The $Cu(OH)_2$/Cu mesh was completely converted into the Cu_2O/Cu mesh electrode after annealing in N_2 atmosphere at 500 ˚C for 4 h. The conversion was presumably obtained by dehydration of $Cu(OH)_2$ to CuO at approximately 120 ˚C [43, 44] followed by removal of oxygen from the lattice of CuO, to transform CuO into Cu_2O at 500 ˚C. The annealing process, which is a green method where no hazardous reductants,[45] are used to result a highly conducting graphene film, also resulted reduction of GO to graphene in the nanocomposite (see Fig. 1a and 1b).

As shown on the XRD patterns of graphite, graphene oxide and graphene (Fig. 1a) the sharp graphitic peak at 2θ value of 26.2 ˚ was completely disappeared after oxidation and a new well defined peak appeared at a diffraction angle of 10.2 ˚. On the other hand, the reduction of GO was confirmed by shift in the diffraction pattern from 10.2 ˚ to 25.6 ˚. The newly emerged peak at 25.6 ˚ resembles that of graphite diffraction pattern. The position of peak shift from 26.2 ˚ to

10.2 ° and vise versa confirms that a complete oxidation of graphite to graphite oxide and complete reduction of GO to graphene respectively.[46]

The oxidation of graphite to graphene oxide and then the reduction of graphene oxide to graphene is further supported by Raman spectroscopy which was used to determine the density of defects in the graphene sheets and investigate the ordered/disordered crystal structures of carbon containing materials.[47] From the Raman spectra (Fig. S1), the change in band shape and band position of D and G peaks and the intensity ratio (I_D/I_G) in the transformation from graphite to GO and GO to graphene clearly confirm oxidation and reduction processes respectively (see detail in the supporting information, Fig. S1 and Table S1).

Fig. 1b shows Raman spectra for bare Cu_2O/Cu mesh, G-1.0/Cu_2O/Cu mesh nanocomposite and graphene. Fig. 1c shows the enlarged Raman spectra of bare Cu_2O/Cu mesh. The nanocomposite (G-1.0/Cu_2O/Cu mesh) and the bare (Cu_2O/Cu mesh) samples showed similar characteristic phonon frequencies of the crystalline Cu_2O. The most intense peak at lower frequency 218 cm^{-1} originated from the second-order Raman-allowed mode of the Cu_2O crystals.[48] Whereas the weak Raman features at 308 and 515 cm^{-1} match well to the second-order overtone mode and the Raman-allowed mode, respectively, and the peak at 635 cm^{-1} is ascribed to the infrared-allowed mode.[49] The absence of characteristic peaks of CuO at 298, 330 and 602 cm^{-1} confirms the two photocathode contain pure Cu_2O crystal without CuO impurities.[50] Relative to the bare Cu_2O/Cu mesh, the band features of the G-1.0 /Cu_2O/Cu mesh nanocomposite get broadened and slightly shifted to the lower frequency region is probably because of the formation of Cu–O–C. That is, the reduction of GO/$Cu(OH)_2$/Cu mesh nanocomposites will result in the formation of Cu_2O/Cu mesh with graphene layer attached onto the surface via Cu–O–C bonds rather than physical contacts. Furthermore, the sharply defined mode at 218 cm^{-1} demonstrates the high structural quality of the synthesized samples, which correlates very well with the X-ray diffraction results.

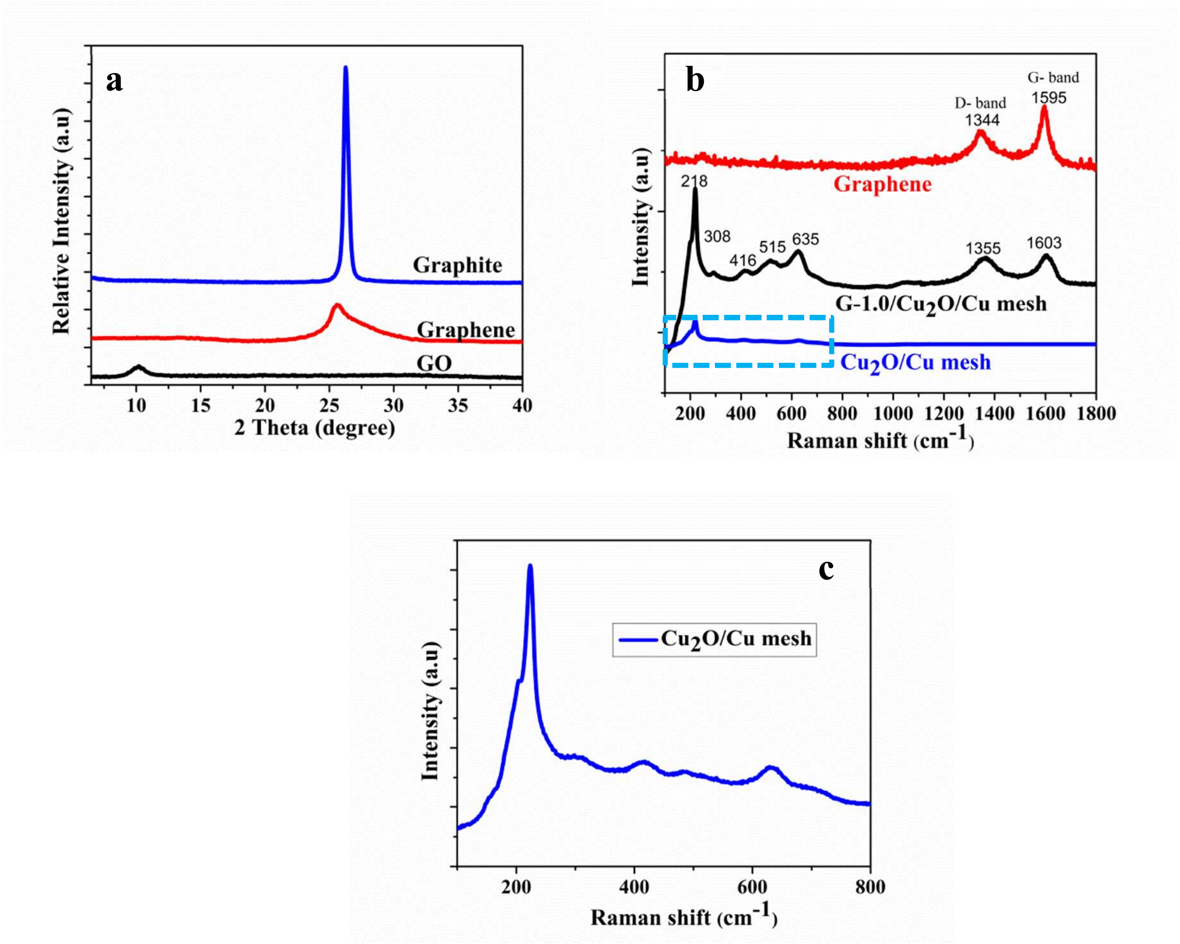

Fig. 1 (a) X-ray diffraction patterns of pristine graphite, graphene Oxide and graphene; (b) Raman spectra of Cu_2O/Cu mesh, G-1.0/Cu_2O/Cu mesh and graphene (c) enlargement of selected portion of blue curve (Cu_2O/Cu mesh) in Fig. 1b

Similar to the pure graphene, the G-1.0/Cu_2O/Cu mesh nanocomposite showed D-band and G-band centered at 1355 and 1603 cm^{-1} respectively (Fig. 1b). As seen from the spectra in Fig. 1b, the nanocomposite achieved lower intensity ratio (I_D/I_G 0.85) than the pure graphene (I_D/I_G 1.31). The higher I_D/I_G ratio of the graphene indicates probably due to the formation of large number of multilayered graphene (thin graphite) through graphene restacking.[51] The G-1.0/Cu_2O/Cu mesh nanocomposite showed much reduced graphene restacking because the Cu_2O/Cu mesh is covered with graphene sheet. As a result the G-1.0/Cu_2O/Cu mesh nanocomposite has less lattice defects than the graphene reduced from the GO. Thus, the decreased number of defect concentration is supposed to provide improved PEC activity of graphene/Cu_2O/Cu mesh photocathode because these lattice defects normally act as recombination centers for the photo-generated electrons and holes. It is worth noting that the G- band position of G-1.0/Cu_2O/Cu mesh showed a red shift that is from 1595 to 1603 cm^{-1}, as compared with that of graphene. This provides reliable evidence of the superior interactions and charge transfer,[52] between graphene and the Cu_2O/Cu mesh in the graphene/Cu_2O/Cu mesh composite.

Fig. 2a and b show the typical low resolution scanning electron microscopy (SEM) image of the original smooth copper mesh substrate and anodized copper mesh substrate respectively. After the galvanometric anodization, a layer of nanostructured $Cu(OH)_2$ was produced on the copper mesh substrate (Fig. 2b). As shown in the scanning electron microscope (SEM) (Fig. 2b) images, the $Cu(OH)_2$ nanowire arrays grew uniformly and densely on the original smooth Cu mesh substrate after anodization. The inset in Fig. 2b confirms blue color of $Cu(OH)_2$ nanowire arrays fabricated on the Cu mesh substrate. The scanning electron microscope image in Fig. 2c clearly shows the $Cu(OH)_2$/Cu mesh is scaffold with the GO sheet. The formation of pure $Cu(OH)_2$ phase with no impurities was confirmed by the use of X-ray diffraction (XRD). Fig. 2d shows the XRD patterns of $Cu(OH)_2$/Cu mesh and GO/$Cu(OH)_2$/Cu mesh nanocomposite. For the $Cu(OH)_2$/Cu mesh sample (blue colored curve in Fig. 2d), all the indexed diffraction peaks except those marked with diamond, which are attributed to the copper mesh substrate(JCPDS card number 04-836), can be indexed to the orthorhombic phase of $Cu(OH)_2$ (JCPDS card number 80-0656), indicating that $Cu(OH)_2$ is well crystallized. Except a very weak intense peak signal at $2\theta = 10.5\ ^\circ$, which gives a hint for the existence of GO, the XRD pattern of the GO/$Cu(OH)_2$/Cu mesh (green colored curve in Fig. 2d) was similar to that of $Cu(OH)_2$. The weak intense GO peak is probably due to the low content and relatively low diffraction intensity GO.

The structures and phase purities of as prepared Cu_2O nanowire arrays were also investigated. Fig. 2e illustrates the XRD patterns of Cu_2O/Cu mesh without graphene (Cu_2O/Cu mesh) (magenta colored curve) and with graphene (G-1.0/Cu_2O/Cu mesh) (blue colored curve) respectively. Both exhibited similar characteristic diffraction peaks of the Cu_2O (JCPDS card number 05-0667). All the peaks marked with circle belong to the Cu^+ with strong intensity along the (111) direction while those peaks marked with diamond belongs to the Cu mesh substrate. This indicates that pure and well crystallized Cu_2O nanostructures with no peak of impurities such as cupric oxides are found in the XRD pattern besides the Cu substrate.[53] It is to note that the G-1.0/Cu_2O/Cu mesh sample principally composed of a cubic Cu_2O and face centered Cu phases and show no clear characteristic diffraction peak for the graphene (blue colored curve in Fig. 2e). This is because of the low amount and relatively low intensity of graphene and probably due to the disappearance of the layer-stacking regularity after redox of graphite.[54] This is in good agreement with the Raman data.

The higher magnification SEM image of $Cu(OH)_2$ nanowires array (Fig. 3a, b) exhibited standing upright and sharp morphology. The SEM images of Cu_2O/Cu mesh without graphene show that the morphology of the nanowires arrays becomes twisted and fractured (Fig. 3c or d) surface after the thermal treatments of the $Cu(OH)_2$ nanowires arrays. That is due to removal of water from $Cu(OH)_2$ and oxygen from the lattice of CuO at higher temperature may cause softening of the core part of the nanowires arrays and as a consequence surface fracturing and twisting to happened. This would be very undesirable for PEC application of Cu_2O given its already high inclination toward photocorrosion.[39] As seen in the SEM images of nanowire arrays architecture (Fig. 3e, f), it is interesting to see that samples with ultrasmooth surface and a uniform dimension could be obtained after incorporating optimized concentration of chemically exfoliated GO sheet (G-1.0/Cu_2O/Cu mesh). To the contrary of Cu_2O/Cu mesh, there was no fracture observed. The morphological difference is clearly attributed to the presence of graphene coating, which kept the integrity of nanowire array during the annealing. In the SEM image displayed in Fig. 3c, d and Fig. 3e, f, the average diameter of bare Cu_2O/Cu mesh and graphene modified Cu_2O/Cu mesh (G-1.0/Cu_2O/Cu mesh) nanowire arrays were 375 nm and 420 nm respectively. The difference in diameter which is approximately 45 nm indicates the graphene coating over Cu_2O/Cu mesh nanowire.

The SEM images of the nanocomposite at low and high concentration of graphene, which is not included here, demonstrates that the minimum graphene concentration for forming a continuous smooth surface coating layer in the current system (G-x/Cu_2O/Cu mesh) is 1.0 mg mL^{-1} while the absence of an extended continuous network of graphene at low GO concentration suggests that a small amount of GO (0.25, 0.50 and 0.75 mg mL^{-1}) was not sufficient to initiate complete attachment with Cu_2O nanowire arrays, resulting surface fracture. On the other hand, any further increase of the graphene concentration beyond 1.0 mg mL^{-1} resulted in the formation of big stone shape like graphene sheets which would absorb visible light at large and as a consequence it decreased the performance of the photocathode materials.

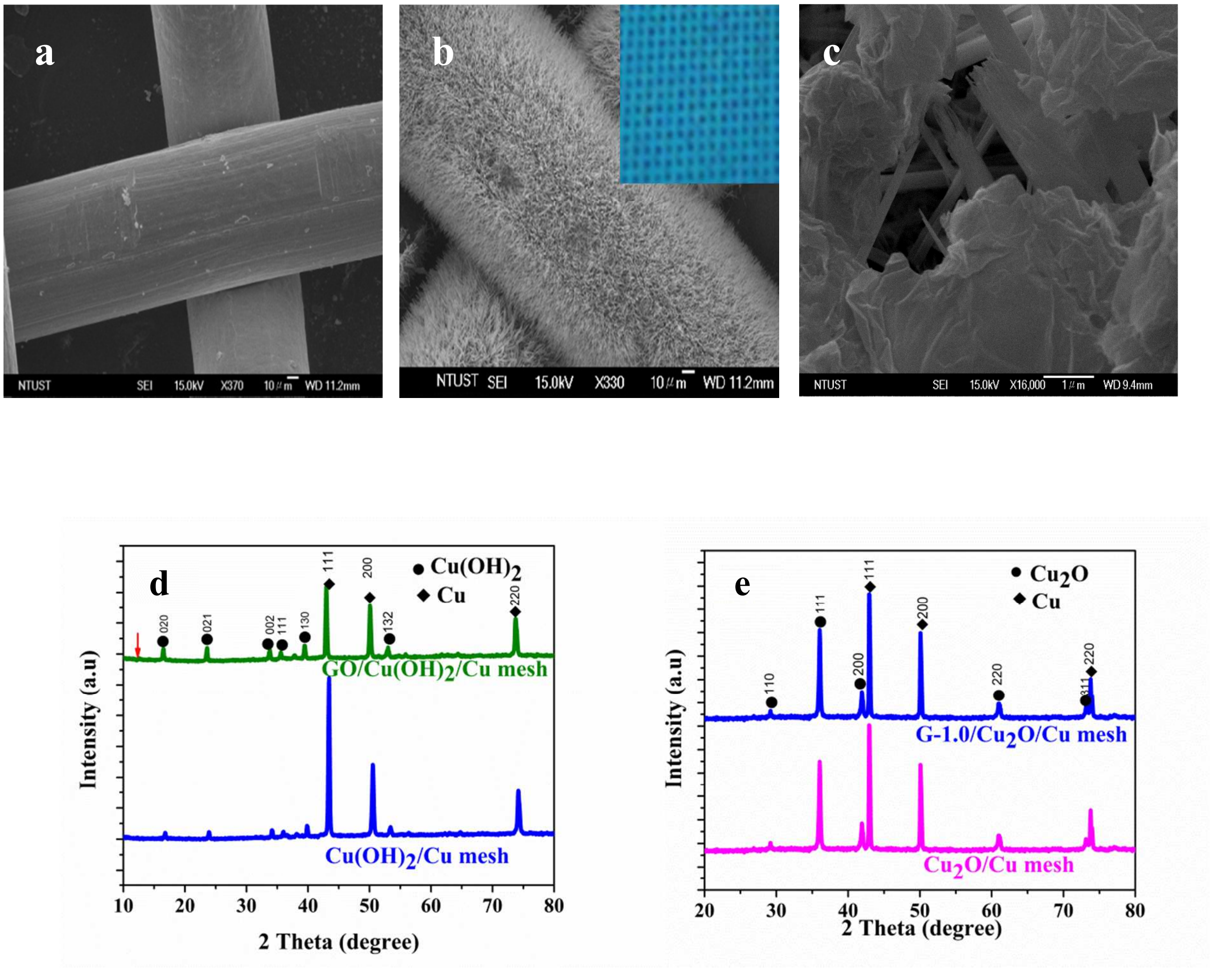

Fig. 2 (a) low magnification SEM images of Cu mesh substrate (b) low magnification SEM images of $Cu(OH)_2$/Cu mesh (c) SEM images of GO/$Cu(OH)_2$/Cu mesh (d) XRD patterns of $Cu(OH)_2$/Cu mesh and GO/$Cu(OH)_2$/Cu mesh (e) XRD patterns of Cu_2O/Cu mesh and G-1.0/Cu_2O/Cu mesh

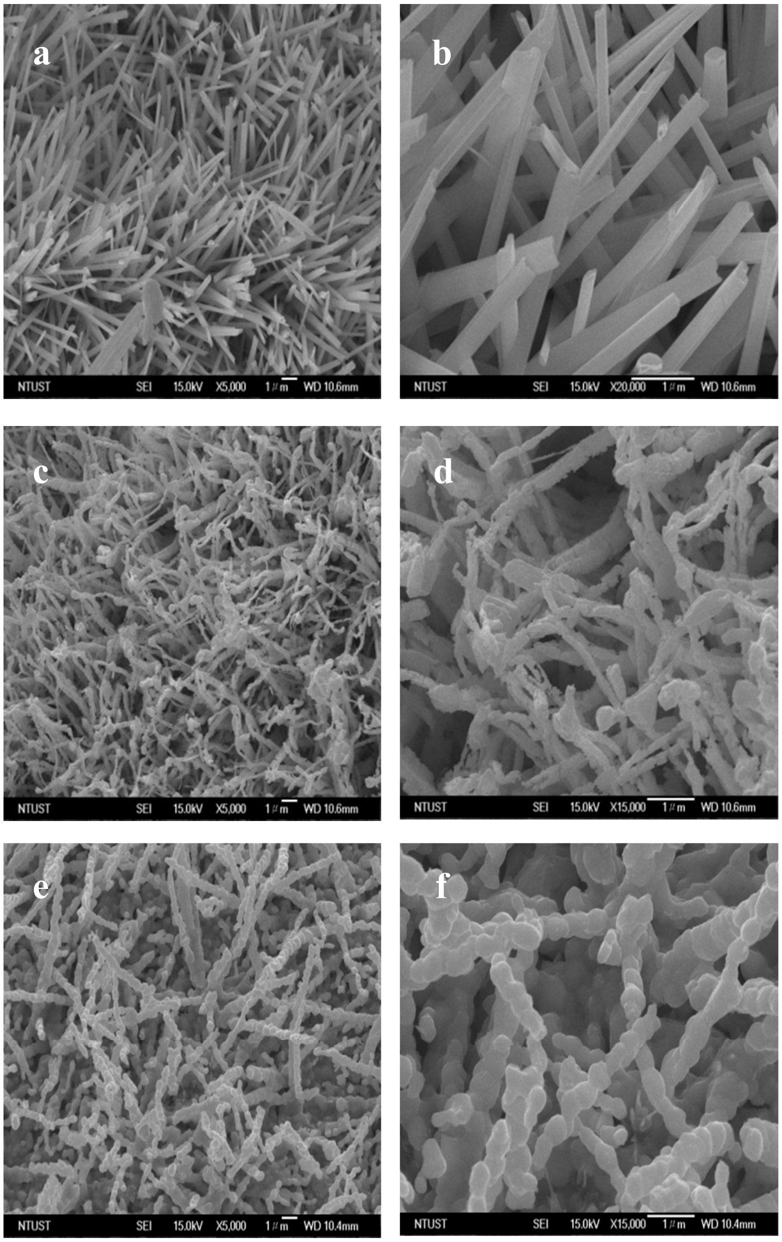

Fig. 3 Scanning electron microscopy images of (a, b); $Cu(OH)_2$/Cu mesh; (c, d) Cu_2O/Cu mesh and (e, f) G-1.0/Cu_2O/Cu mesh

The extent of reduction of GO to graphene in nanocomposits using thermal reduction process was investigated by high-resolution XPS. Fig. 4a shows the X-ray photoelectron (XPS) spectra of C1s collected from GO/$Cu(OH)_2$/Cu mesh and G-1.0/Cu_2O/Cu mesh samples, whereas the XPS survey spectra for $Cu(OH)_2$/Cu mesh, GO/$Cu(OH)_2$/Cu mesh and G-1.0/Cu_2O/Cu mesh, are shown in Fig. S2a (supplementary information). As shown in Fig. 4a, the deconvolution of the C

1s of GO/$Cu(OH)_2$/Cu mesh peak demonstrates four peaks (colored lines) located at binding energies of 284.7, 286.3, 288.1, and 290.2 eV, which can be attributed to the C–H, C–C, C=C (sp^2 bonded carbon), C–O (hydroxyls /epoxy), C=O (carbonyls), and O–C=O (carboxyl) functional groups, respectively.

Even though the C 1s XPS spectra of G-1.0/Cu_2O/Cu mesh (Fig. 4b) exhibited the same oxygen-containing functional groups as C 1s of GO/$Cu(OH)_2$/Cu mesh, the intensity of most peaks was much lowered compared with peaks in GO. In addition, the increased in percentage of graphitic carbon from 39.1% to 60.9% indicating the loss of oxygen containing functional after the thermal reduction process. These results indicate that about 64% of the oxygen-containing functional groups were removed during thermal reduction process.

The chemical composition of $Cu(OH)_2$/Cu mesh, GO/$Cu(OH)_2$/Cu mesh and G-1.0/Cu_2O/Cu mesh were further investigated by XPS to examine the change in chemical status of Cu atom. The core level spectra of Cu 2p peaks of $Cu(OH)_2$/Cu mesh at 934.4 and 954.2 eV (black line in Fig. S2b and GO/$Cu(OH)_2$/Cu mesh at 935.5 and 955.5 (red line in Fig. S2b) corresponded to Cu $2p_{3/2}$ and $2p_{1/2}$ respectively, indicating an oxidation state of copper 2+. The formation of Cu^{2+} on the copper mesh surface was further evidenced by the appearance of shake-up satellite peaks of the $Cu(2p_{3/2})$ and $Cu(2p_{1/2})$ at relatively higher binding energy, 942.9 and 954.2 eV for $Cu(OH)_2$/Cu mesh and 943.4 and 955.4 eV for GO/$Cu(OH)_2$/Cu mesh, respectively.

On the other hand, as shown in Fig. 4c, the binding energies of 932.4eV and 952.2eV match well with the $Cu2p_{3/2}$ and $Cu2p_{1/2}$ peaks of Cu^+ respectively.[32] The disappearance of satellite peak at 942.3 eV and the shift in Cu $2p_{3/2}$ and $2p_{1/2}$ peaks of GO/$Cu(OH)_2$/Cu mesh to the low-energy values 932.4 and 952.2 eV further confirmed thermal reduction of Cu^{2+} species (GO/$Cu(OH)_2$/Cu mesh or $Cu(OH)_2$/Cu mesh) to Cu^+ at the annealing temperature of 500 ˚C. Therefore, it can be concluded from both XRD patterns, Raman and XPS spectrum that Cu_2O was the only reduced product from $Cu(OH)_2$ and there was no CuO impurities.

O 1s spectra of the samples were also recorded with XPS. The O1s lines of $Cu(OH)_2$/Cu mesh and GO/$Cu(OH)_2$/Cu mesh (Fig. S2c) are centered at 530.95 and 531.81 eV respectively. The positive shift of both the O 1s and Cu 2p (see Fig. S2b and Fig. S2c) confirms the formation of

Cu–O–C bond, which is in good agreement with our Raman measurements. Furthermore, as shown in Fig. S2c, the binding energy of O1s peak position at 531.10 eV is the conclusive XPS evidence of the formation of Cu_2O during the thermal reduction process. Therefore, data from Raman and XPS provide strong evidence of the establishment of a Cu–O–C bond.

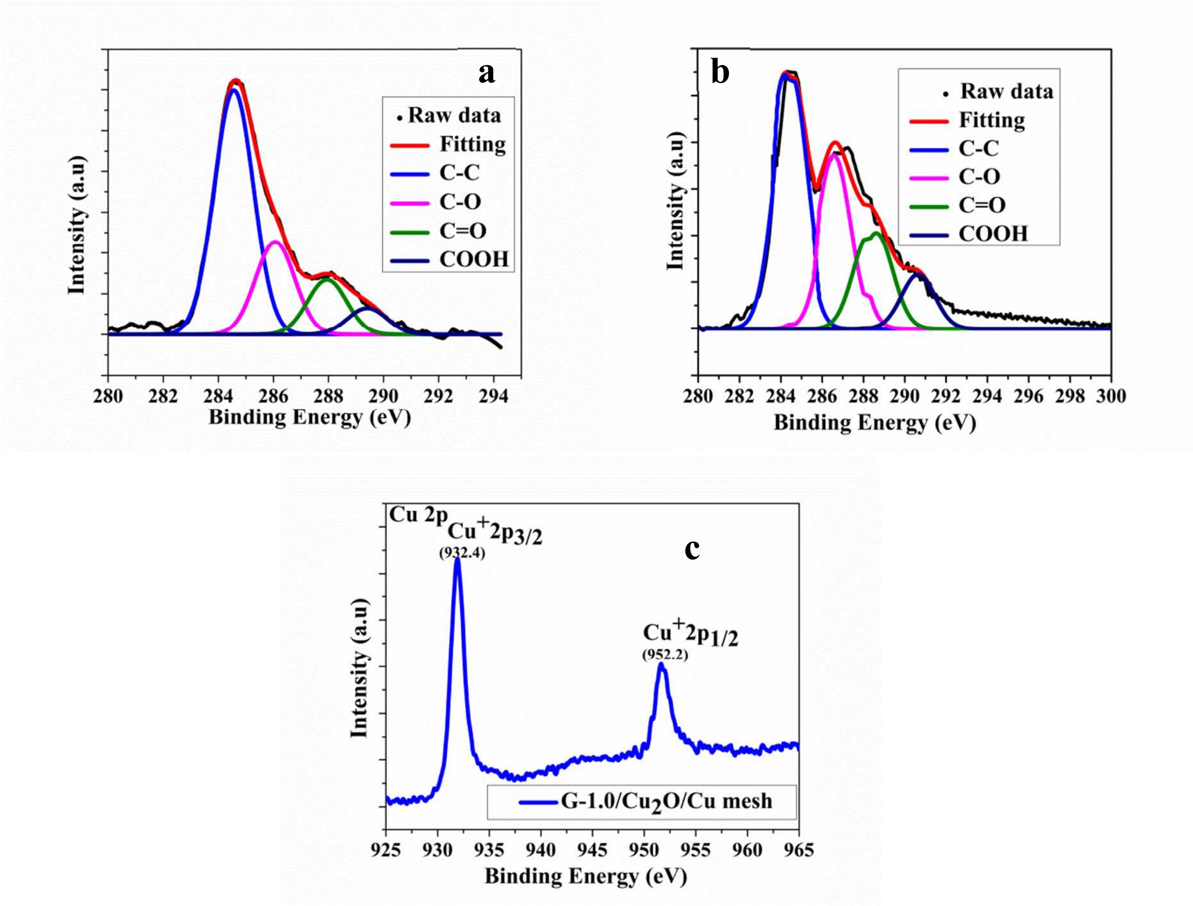

Fig. 4 XPS spectra of: (a) C 1s core level of GO/$Cu(OH)_2$/Cu mesh (b) C 1s core level of G-1.0/Cu_2O/Cu mesh (c) Cu 2p core level of G-1.0/Cu_2O/Cu mesh

The G-1.0/Cu_2O/Cu mesh was further characterized using transmission electron microscopy (TEM) and high-resolution transmission electron microscopy (HRTEM). The TEM image shown in Fig. 5a suggests that the Cu_2O NWAs were wrapped in thin and transport graphene sheet layer. This distinctive structure feature offers an intimate interface between the Cu_2O/Cu mesh NWAs and graphene, which can be helpful for the suppression of self photocorrosion of the photocathode material and improving the charge separation and thus the PEC activity. A HRTEM image of G-1.0/Cu_2O NWAs wrapped with graphene was shown in Fig. 5b and c.

In a HRTEM images (Fig. 5b and c) obtained from the selected area shown in Fig. 5a, the presence of continuous lattice fringes throughout the structure were revealed and confirmed the existence of lattice planes and good crystallinity. The observed lattice fringe spacing of 0.247 nm (Fig. 5b) is characteristic and match well with the (111) plane of Cu_2O. The lattice fringe shown in Fig. 5c is also a characteristic graphitic lattice with an interplanar distance of 0.34 nm, corresponding to the spacing of the (002) planes. This indicates that the HRTEM result is consistent with XPS, XRD and Raman data's verifying the reduction of the GO to graphene together with the formation of Cu_2O crystals. The selected area electron diffraction patterns (SAED) shown in inset in Fig. 5b clearly related to a set of diffraction rings due to the polycrystalline Cu_2O.

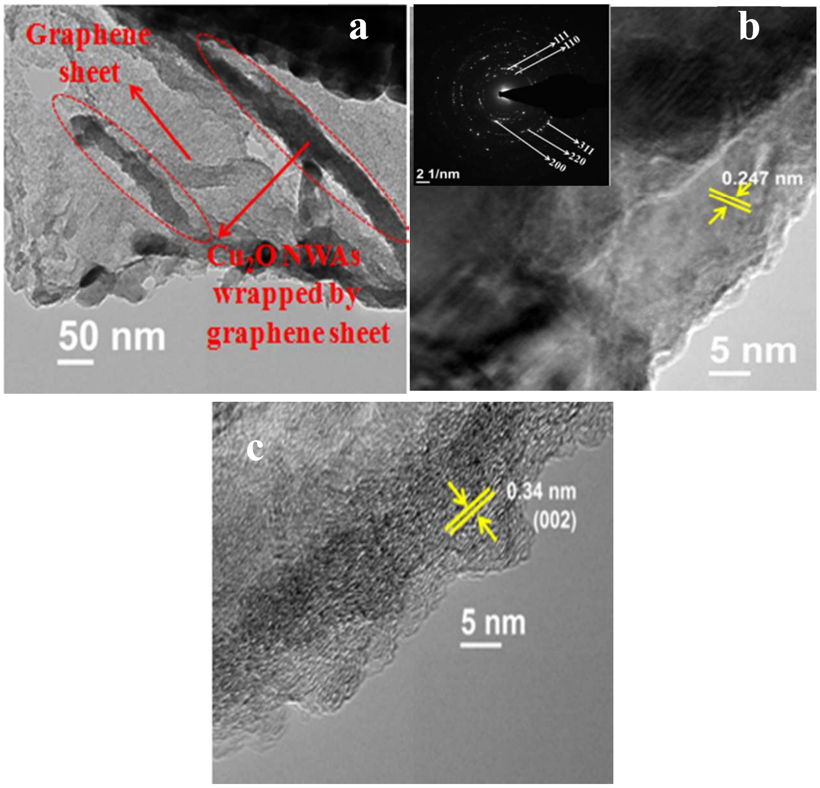

Fig. 5 (a) TEM image of G-1.0/Cu_2O/Cu mesh, (b) HRTEM images of Cu_2O in G-1.0/Cu_2O/Cu mesh composite and corresponding SAED patterns (inset) and (c) HRTEM images of graphene in G-1.0/Cu_2O/Cu mesh.

In order to realize the effect of graphene on the photoresponse of the as-prepared G-x/Cu_2O/Cu mesh (x = 0.25, 0.5, 0.75, 1.0, 1.5 and 3.0 mg mL^{-1}), the optical properties of these samples were measured with UV–vis diffuse reflectance spectra (DRS). Fig. 6a and 6b shows UV–vis absorption spectra's of bare Cu_2O/Cu mesh, G-1.0/Cu_2O/Cu mesh samples and their corresponding Tauc plots respectively. The maximum absorption of light revealed by both the samples (see Fig. 6a) in the short wavelength region (300–600 nm) can be related to the intrinsic band gap of Cu_2O/Cu mesh. The optical absorption of G-1.0/Cu_2O/Cu mesh nanocomposite in the visible region (620–800 nm) was higher than that of the bare Cu_2O/Cu mesh. This indicates, the incorporation of graphene is able to effectively promote the visible light response of the graphene/Cu_2O/Cu mesh nanocomposites. As shown in Fig. S3, similar phenomenon was revealed on all the G-x/Cu_2O/Cu mesh samples, where the gradual increase in concentration of graphene increased the absorption in the visible region. This is also observed as a color change of the samples, which became from shiny red to dark red (see digital photograph of the nanostructures under scheme 1e and 1d). This confirmed the existence of graphene in the graphene/Cu_2O/Cu mesh, which reduces reflection of light and thus enhances the absorption.[55]

Fig. 6b indicates estimation of the band gap energy, which is the same for both bare Cu_2O/Cu mesh and G-1.0/Cu_2O/Cu mesh (2.03 eV), by extending the straight part of the $(\alpha h\nu)^2$ versus photon energy ($h\nu$) curve to $\alpha = 0$ using Kubelka−Munk function.[56] In addition to this, close inspection shows that all the graphene/Cu_2O/Cu mesh samples showed almost the same absorption edge as that of the unmodified Cu_2O/Cu mesh. This demonstrates that band gap narrowing did not occur in the existence of graphene and thus it confirms that graphene was not incorporated into the lattice of Cu_2O/Cu mesh.

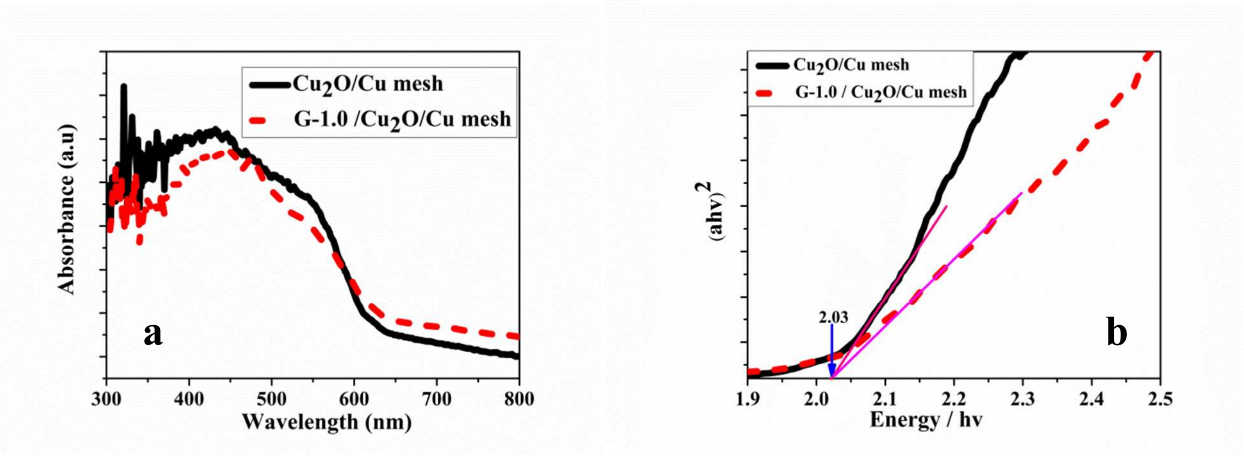

Fig. 6 Photo-optical characteristics of Cu_2O/Cu mesh and G-1.0/Cu_2O/Cu mesh samples, (a) UV–Vis diffuse reflectance spectra; (b) Tauc plot

The PEC properties of the bare Cu_2O/Cu mesh and graphene modified Cu_2O/Cu mesh are given in Fig. 7. Fig. 7a and 7b shows the current–potential curves (LSV measurement) of bare Cu_2O/Cu mesh and graphene modified Cu_2O/Cu mesh measured under the same conditions respectively. The linear sweep voltammetry measurement were recorded under chopped illumination, which simultaneously shows dark current and photocurrent in a single sweep, of the as-prepared photocathode materials in this study. The LSV measurement of the G-1.0/Cu_2O/Cu mesh sample (Fig. 7b) at water reduction potential (0 V vs RHE) produced the photocurrent density of– 4.8 mA cm^{-2}, which is the maximum value of all the samples, and is more than two times higher than the photocurrent density of bare Cu_2O/Cu mesh (–2.3 mA cm^{-2} Fig. 7a).

More interestingly, the measured photocurrents densities in bare Cu_2O/Cu mesh photocathode are 0.7–0.2 mA cm^{-2} at higher applied potential range of 0.2 – 0.4 V vs RHE. However, at the same range of applied bias, the obtained photocurrents density 2.1–1.1 mA cm^{-2} drastically increased in G-1.0/Cu_2O/Cu mesh sample (Fig. 7b). This represents an increase of 300–550% compared with the bare Cu_2O/Cu mesh sample. Being able to achieve high photocurrent density at more positive voltage for a photocathode would lessen the voltage requirement from the photoanodes and significantly improve the water splitting efficiency.[57]

This enhancement of photocurrent density is believed to be ascribed to the synergetic interaction of graphene sheet over Cu_2O/Cu mesh towards the light absorption tendency together with the photocathode and its excellent property as electron acceptor and mediator.[58] Graphene facilitates the photoexcited electron transfer at the site of generation from the Cu_2O surface and thereby leads to a reduced recombination of electron and hole.[59] In addition, the much improved PEC activity exhibited by G-1.0/Cu_2O/Cu mesh than bare Cu_2O/Cu mesh is due to the improved crystallinity of 1D nanowire arrays by incorporating graphene, which were expected to have efficient light absorption and carrier collection, reduced reflection, and large surface area for reaction.[60]

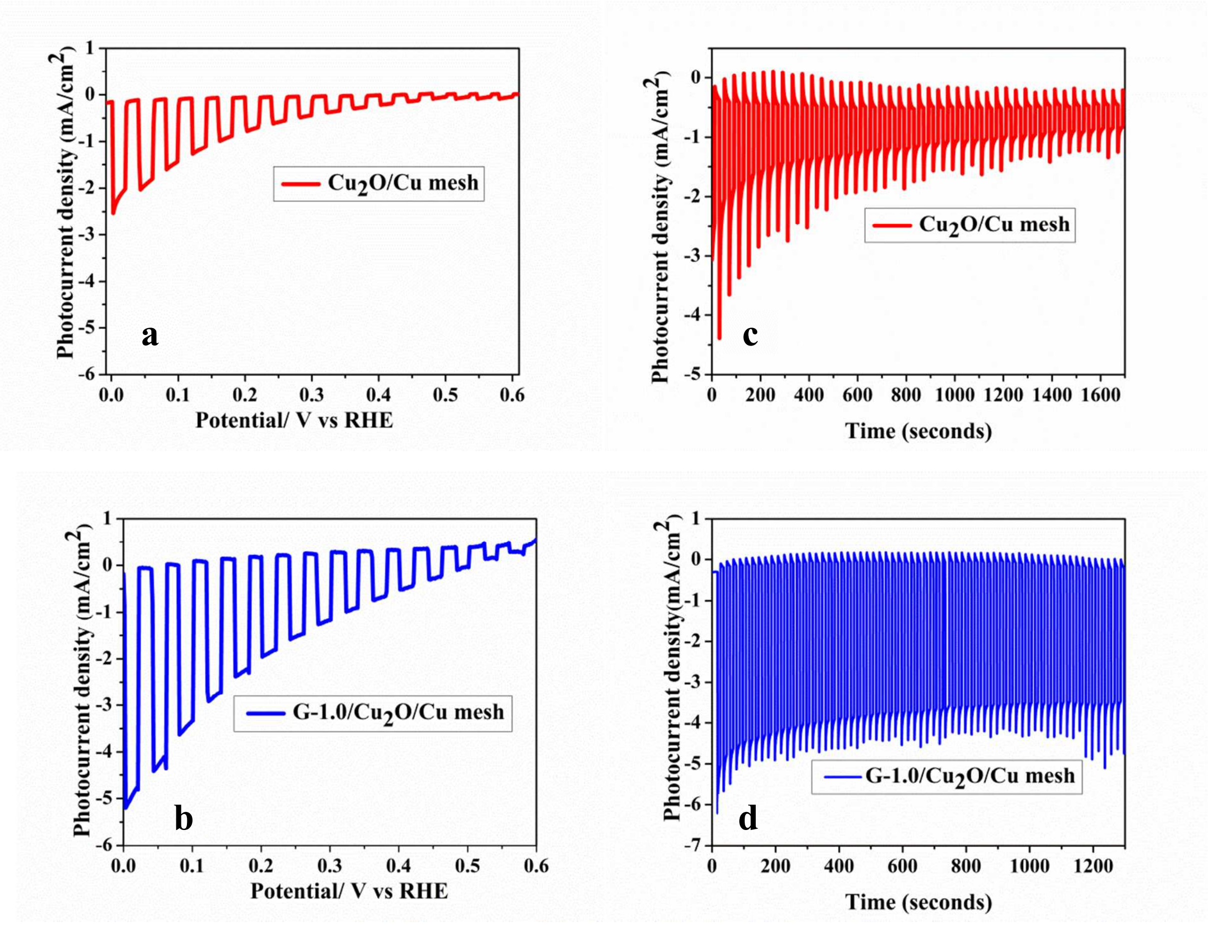

Fig. 7 PEC performances and stability measurement of (a, c) Cu_2O/Cu mesh and (b, d) G-1.0/Cu_2O/Cu mesh

To examine the stability of photocathode material, chronoamperometric measurements was employed under illumination at 0 V vs RHE in light on/off cycle. The photostability was quantified as the percentage of the photocurrent density at the end of the last light cycle (J) compared with that at the end of the first light cycle (J_0) within the 20 min measurement period.[38, 39, 61] As shown on Fig. 7c, the bare Cu_2O/Cu mesh, which exhibited maximum photocurrent density (–2.3 mA cm^{-2}) for the first few seconds rapidly get decayed with generating current spikes on the on-off cycle. As clearly seen in Table1, the photocurrent density as well as photostability gradually increased as we incorporated successive concentration of graphene to the Cu_2O/Cu mesh up to 1 mg $mL^{-1}$and we found that G-1.0/Cu_2O/Cu mesh nanocomposite exhibited the highest photocurrent density (–4.8 mA cm^{-2}) with efficient photostability. On the other hand, when the electrode is made in graphene concentration higher than 1.0 mg mL^{-1}, the PEC performance of the photocathode is the worst experiencing formation of spikes (Fig. S4 I-t curves, f-j). The observed decrease in photocurrent density was due to the competition of absorption of visible light by graphene and the semiconductor.

Table 1 Effects of graphene concentration on photocurrent density and stability of G-x/Cu_2O/Cu mesh sample

Sample	**Graphene concentration (mg mL^{-1})**	**Photocurrent density (mA cm^{-2})**	**Stability % (J/J_o) after 20 minutes**
Bare Cu_2O/Cu mesh	0.00	–2.3	14.5
G-0.25/Cu_2O/Cu mesh	0.25	–2.6	32
G-0.50/Cu_2O/Cu mesh	0.50	–3.0	35
G-0.75/Cu_2O/Cu mesh	0.75	–3.5	86
G-1.0/Cu_2O/Cu mesh	1.0	–4.8	83.3
G-1.5/Cu_2O/Cu mesh	1.5	–2.0	85
G-3.0/Cu_2O/Cu mesh	3.0	–1.5	23.5

Also the percentage of photocurrent density of the prepared photocathodes at the end of 20 minutes was determined. The photocurrent density of G-1.0/Cu_2O/Cu mesh (Fig. 7d) at the end of 20 minute showed more than five times higher photostability (83.3%) than the bare Cu_2O/Cu mesh (14.5 %). This demonstrates graphene provides an excellent behavior in suppressing photocorrosion of Cu_2O and also serves as a fast transferring of the photoinduced carriers and a low recombination rate of electron-hole pairs. The PEC performances of all the other samples were summarized and displayed in Table 1 and Fig. S4 respectively

The photostability of G-1.0/Cu_2O/Cu mesh photocathode in continuous irradiation during Hydrogen experiment was showed in Fig. S5. Meanwhile, compared with the measured photocurrent density of G-1.0/Cu_2O/Cu mesh during chopping of light (Fig. 7d) and in the continuous irradiation (Fig. S5), the G-1.0/Cu_2O/Cu mesh showed slight decrease in photocurrent density in the continuous irradiation. This is probably due to the partial decomposition of graphene by the photogenerated holes during a long time of continuous irradiation.[62, 63]

Faradaic efficiency, which is the ratio of the total amount of charge Q(C) passed through the system to the total amount of hydrogen produced nH_2 (mol),[64] was also determined to examine the photostability of Cu_2O based photocathodes and to conform whether the resulted cathodic photocurrent density is from water reduction or self photoreduction of Cu_2O to Cu.

The amount of H_2 evolved for the investigation of the Faradaic efficiency was determined with a gas chromatograph (see details in the supportive information, Fig. S7). After passing 5.4 C (Fig. S6) through the G-1.0/Cu_2O/Cu mesh photocathode at 0 V vs RHE under continuous standardized solar-light illumination, an amount of 0.0207mmole H_2 was detected, corresponding to a Faradaic efficiency of 74%. The deviation in Faradic efficiency from unity indicating that part of the photocurrent density is used in photoreduction of Cu_2O. However, the corrosion of electrode surface is not so clearly evident both on SEM image, XRD, XANES and EXAFS characterization after photostability measurement (see detailed description in the next section). Thus, the efficiency of H_2 evolution was less than 100%, possibly due to unwanted backward reaction between H_2 and O_2,[65] gas leakage or dissolution in the electrolyte solution.[66] In spite of these limitations, the result of the present study reveals that the graphene modified Cu_2O photocathode exhibit suppressed photocorrosion property over the unmodified Cu_2O photocathode. That is under similar condition the bare Cu_2O/Cu mesh photocathode did not showed measurable amount of H_2 gas after continuous AM1.5 illumination for 20 min at an applied potential of 0 V vs RHE. This indicates that the generated photocurrent density is due to the self photoreduction of Cu_2O to Cu. This is in good agreement with literature reports before.[13, 15] To get evidence, we carried out post characterization (after PEC test) for both bare and graphene modified photocathode with XRD, scanning electron microscope (SEM), EXAFS and XANES. To make it clear, the as prepared samples were cut into two parts. One part was taken to XRD, SEM, XANES and EXAFS characterization directly and the other part was taken into post characterization after photostability measurement.

As shown in SEM image in Fig. S8 and in the inset digital photograph, the irradiated surface of the bare Cu_2O photocathode exhibited severe surface change resulting Cu particles, identified by formation of visible black spots (inset digital photograph in Fig. S8b) over the surface of Cu_2O/Cu mesh sample. The existence of Cu nanoparticles on the surface of Cu_2O/Cu mesh was further confirmed by X-ray diffraction. As shown in Fig. S9a, the XRD measurement after PEC test revealed diminished crystalinity of Cu_2O. To further highlight this effect, the average crystallite sizes of Cu_2O and Cu along the (111) facet diffraction peak were estimated using the Scherrer formula. After photostability measurement for 20 minutes, the average crystallite size of Cu_2O decreases from 30 to 13 nm while it increases from 41 to 48nm in case of Cu, suggesting self reduction of Cu_2O to Cu. However, the absence of copper particles in SEM images (Fig. S8d) and almost the same crystallite size of Cu along the (111) facet diffraction peak after photostability measurement by the graphene modified Cu_2O (G-1.0/Cu_2O/Cu mesh) sample depict the suppressed photoreduction and the enhanced photostability of Cu_2O due to the presence of graphene (see further explanation in the supportive information).

Both SEM and XRD measurements confirmed that photodegradation was a severe problem at bare Cu_2O nanowire arrays/electrolyte interface. Unlike the bare Cu_2O nanowire arrays, the graphene modified Cu_2O showed no significant difference in XRD pattern before and after PEC test (see Fig. S9b). Thus, the present investigation indicates incorporating graphene exhibit interesting protection towards suppressing photocorrosion of Cu_2O and thus increases the photocurrent density and photostability.

To understand more, Cu K-edge XANES measurements were also carried out on bare Cu_2O/Cu mesh and G-1.0/Cu_2O/Cu mesh both before and after photostability test measurement. The Cu near edge XANES spectra for these samples have been superimposed in Fig. 8. As can be seen, the recorded XANES spectra showed little variation between the spectra both in terms of absence of pre-edge peak, the edge height and the position of edge peak. This demonstrates good sample-to-sample consistency.

That is, in all the sample the appearance of more intense peak (peak B1 in Fig. 8a) which is ascribed to the transition of 1s to $4p_{xy}$, reduced intensity of peak C1 (in Fig. 8a) to the transition of 1s to $4p_z$ and disappearance of weak but characteristic pre edge peak in most Cu(II) compounds (peak A in Fig. 8) could be regarded as a signature for a pure univalent copper.[67] This is in good agreement with our XRD, Raman and XPS measurement, confirming the formation of copper +1. Thus, based on the XANES spectra analysis, we could suggest that the as-prepared sample ($Cu(OH)_2$) under thermal treatment in N_2 atmosphere (500 ˚C) was able to completely transform into pure cuprous oxide both in the absences and/or presences of graphene oxide. The peak intensities of the graphene modified sample (G-1.0/Cu_2O/Cu mesh) were slightly less than that of the bare Cu_2O/Cu mesh probably due to different chemical environments caused by interaction of graphene and Cu_2O structure. This is consistent with our Raman and XPS result. There was no obvious change of the peak positions or intensities in XANES after PEC test for 20 minutes, implying that the state of the Cu_2O structure did not showed significant change after PEC test. This is probably because XANES cannot probe the local structural environment of the absorbing atom, however clear change is observed in EXAFS spectra displayed in Fig. 8c.

The Cu-*K* edge FT-EXAFS spectra presented in Fig. 8c look similar, exhibiting two main peaks below 3.5 Å. A broad and slightly an intense peak at 2.4 Å (Fig. 8c) matches well with Cu–Cu bonds whereas the second peak centered at 1.5 Å is due to Cu–O bonds of Cu_2O, consistent with previous reports.[68] The Cu–Cu bond in Cu_2O/Cu mesh after PEC test shifted towards longer bond distance (red curve in Fig. 8c) indicating that the bare Cu_2O undergo structure degradation after photostability test, however the graphene modified Cu_2O showed stable structure feature after PEC test. Furthermore, the decreased in intensity of the Cu-Cu bond distance in bare Cu_2O/Cu mesh after PEC is a good indication of decrease in crystallite size of Cu_2O. This is consistent with our XRD result.

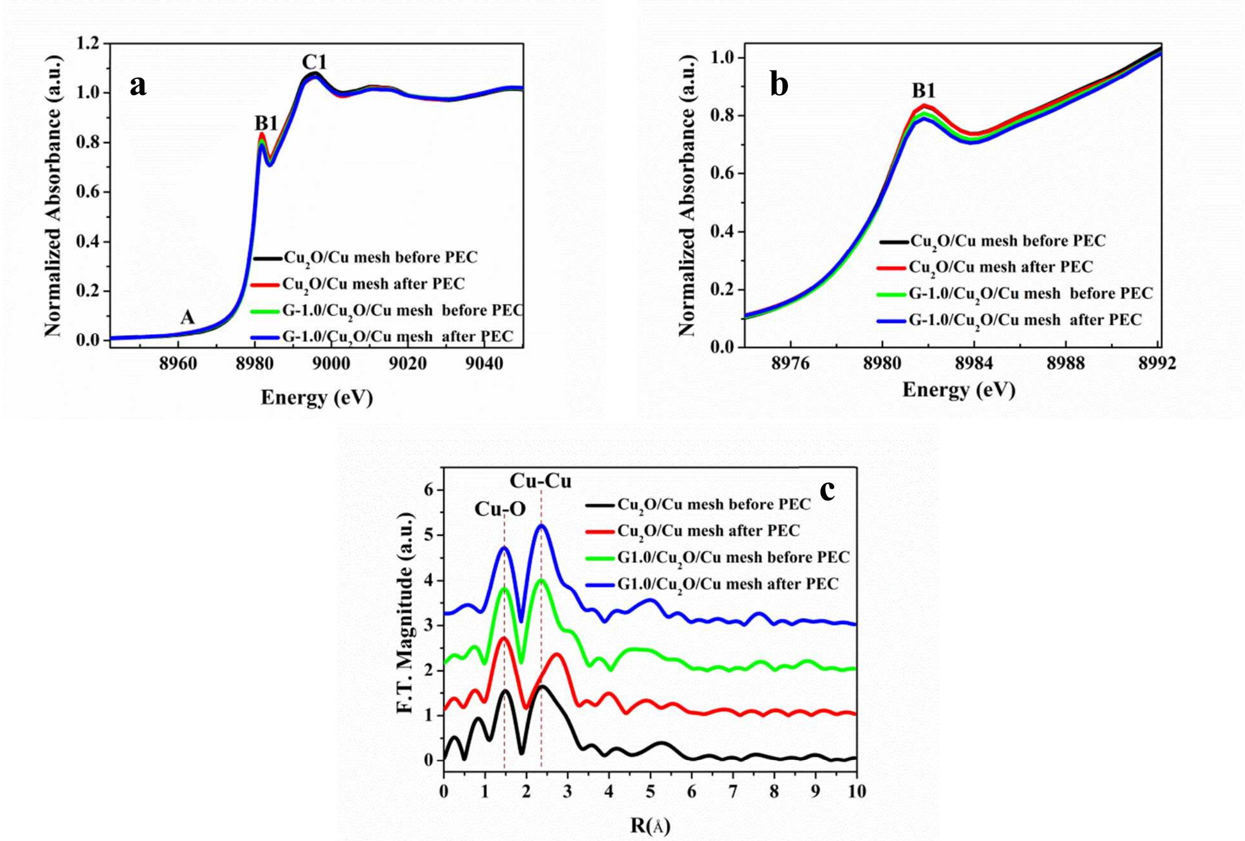

Fig. 8. Cu K-edge XANES spectra of (a) Cu_2O/Cu mesh and G-1.0/Cu_2O/Cu mesh both before and after PEC, (b) enlargement of peak B1 in Fig. 8a (c) Cu K-edge FT-EXAFS spectra of Cu_2O/Cu mesh and G-1.0/Cu_2O/Cu mesh both before and after PEC

We also determined the applied bias photon –to- current efficiency (ABPE), which reveals the solar energy conversion efficiency with the electric energy deducted from the total efficiency, in two electrode systems by applying a bias between working and counter electrodes. The ABPE was estimated using the following expression:[69]

$$\mathrm{ABPE} = \left[\frac{|\mathrm{J_{ph}}|(\mathrm{mA/cm^2}) \times (1.23 - |\mathrm{V_b}|)(\mathrm{V})}{\mathrm{P_{total(mW/cm^2)}}}\right]_{\mathrm{AM\ 1.5G}}$$

Where j_{ph} is the photocurrent density obtained under an applied bias Vb between the working and the counter electrode, 1.23 V is the standard water splitting reaction potential and P_{total} is the incident light intensity (which is 100 mW cm^{-2} in our case). As shown in Fig. S 10c, the G-

1.0/Cu_2O/Cu mesh showed maximum solar conversion efficiency (ABPE), 3.3%, at an applied bias of –0.55 V vs Pt counter electrode (Fig. S10a) (see further information in the supporting information, Fig. S10). The effect of incorporating graphene in accepting and transporting the photogenerated electrons from the semiconductor was evaluated by using electrochemical impedance spectroscopy (EIS), a prominent technique for studying the photoelectrochemical properties of the photoelectrodes. The Nyquist plots of the photocathode modified with 1.0 mg mL^{-1} of graphene (G-1.0/Cu_2O/Cu mesh) and bare photocathode (Cu_2O/Cu mesh) under standardized solar-light illumination and dark conditions are displayed on Fig. 9. The semicircular feature of the Nyquist plots (Fig. 9) at high frequencies is the defining characteristic of the charge transfer process and the diameter of the semicircle is equal to the charge transfer resistance (R_{ct}).[70] For both photocathodes (Cu_2O/Cu mesh and G-1.0/Cu_2O/Cu mesh), the resistance under light was much lower than that in the dark because of the higher charge carrier densities induced by photo-excitation. The charge transfer resistance (R_{ct}) of G-1.0/Cu_2O/Cu mesh was much smaller both in dark and illumination than the bare Cu_2O. This might be due to the incorporated graphene into the Cu_2O/Cu mesh which better facilitate accepting and transferring the photogenerated electron from the semiconductor to the electrolyte and thus enhance the electron conductivity to achieve better photoresponse. In other words, integrating graphene with Cu_2O/Cu mesh enhanced the suppression of electron-hole recombination rate which reflects better photoelectrochemical performance of G-1.0/Cu_2O/Cu mesh photocathode.

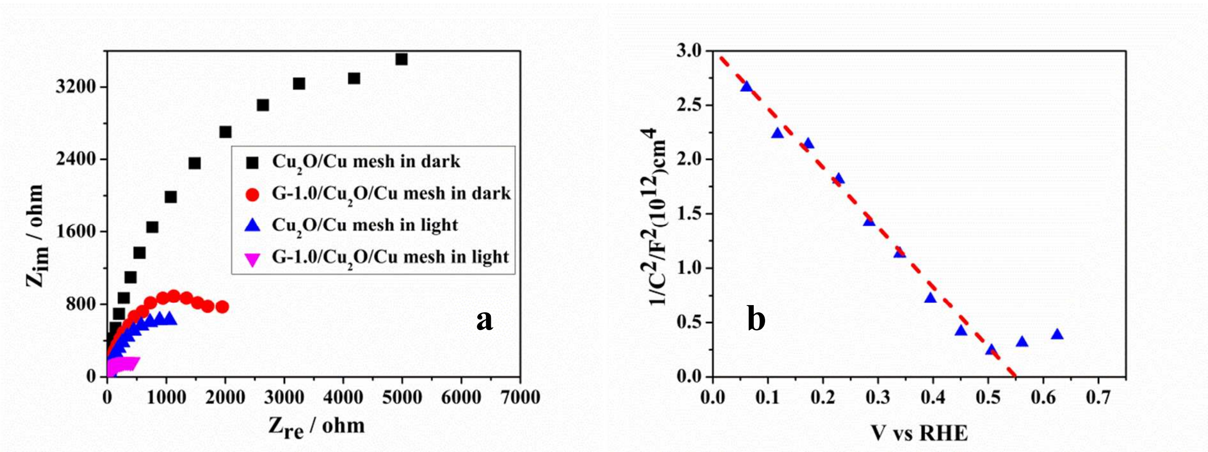

Fig. 9 (a) Nyquist plots of Cu_2O/Cu mesh and G-1.0/Cu_2O/Cu mesh nanowire arrays based photocathodes both in dark and under AM 1.5 illumination in 1.0 M Na_2SO_4 electrolyte buffered at pH 5.0 (b) Mott–Schottky plot

The Mott-Schottky (MS) plot which is 1/C^2 vs. potential Fig. 9b) at a fixed frequency of 1 kHz was employed to investigate the flat band (V_{fb}) and carrier density (N_A). The capacitance-potential measurements on G-1.0/Cu_2O/Cu mesh are presented as a MS plot following the equation below:

$$\frac{1}{C^2} = \frac{2}{\varepsilon_o \varepsilon e N_A A^2}\left(V - V_{fb} - \frac{k_B T}{e}\right) \qquad (1)$$

In equation 1 above, C is the space-charge capacitance of the semiconductor; ε_o is the permittivity in vacuum, ε is the dielectric constant of Cu_2O (taken as 7.6)[71], e is the electronic charge, V_{fb} is the flat-band potential, V is the applied potential, N_A is the number density of acceptors in Cu_2O, T is the absolute temperature, A is area of the electrode and k_B is the Boltzmann constant. The flat band potential (V_{fb}) is determined (equation 2 below) after the small thermal correction (k_BT/e) of the intercept (V_o)[72] which is estimated from extrapolating the linear part of the curve to 1/C^2 equals to zero on the potential axis.

$$V_{fb} = V_o + \frac{k_B T}{e} \qquad (2)$$

The carrier density (N_A), was calculated from the slopes of the Mott-Schottky plots:

$$N_A = \frac{2}{\varepsilon \varepsilon_o S e A^2} \qquad (3)$$

As shown in Fig. 9b, the slope of the linear part of the curve in the Mott-Schottky plot is negative, implying a p-type semiconductor which is in good agreement with the cathodic photocurrent density generated from the photocathodes in our study. Accordingly, the value of carrier concentration estimated from the slope and the flat band potentials obtained from extrapolating the linear part of the curve to 1/C^2 equals to zero on the potential axis at 1 kHz frequency were 3.54 x10^{18} cm^{-3} and 0.58 V vs RHE respectively. The flat-band potential from the Mott−Schottky experiment is consistent with the onset potential which is about 0.6 V. It is reported elsewhere that the flat band potential corresponds to or can be a reasonable approximation of the potential of the valence band[73, 74], thus, the deduction of the optical band gap energy (2.03 obtained from DRS Uv-vis measurement) from the valence band edge (E_V 0.58 V vs RHE) give rise to a conduction band edge of (E_C – 1.45 V vs RHE).

At last, we come across with a tentative scheme that illustrates the conduction and valence band alignments diagram of Cu_2O together with reduction and oxidation potential of water. As shown on Scheme 2, Cu_2O showed suitable energy band positions for water reduction. That is the conduction band of Cu_2O is more negative than the hydrogen evolution potential and the valence band lying just slightly above the oxygen evolution potential. Cu_2O can be exited with visible light illumination to generate electron and holes. As a consequence, the photogenerated electrons move from the valence band to the conduction band of Cu_2O and then transfer to graphene sheet. Finally, the reaction between the adsorbed H^+ ions with photogenerated electrons will result in the evolution of hydrogen gas, whereas the photo-generated holes will be transported to counter electrode to perform oxygen evolution.

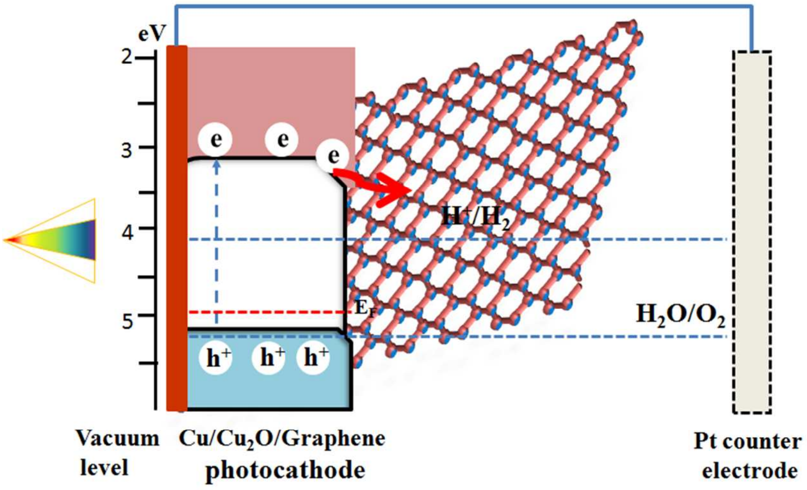

Scheme 2 Proposed energy band alignment of graphene/Cu_2O/Cu mesh nanocomposite electrode

Conclusion

To summarize, we have proposed a low cost, simple and scalable graphene modified 1D Cu_2O based photocathode for highly efficient water reduction. The poor photostability of Cu_2O nanowire arrays due to self photocorrosion was significantly improved by incorporating optimized amount of graphene. Compared to the bare Cu_2O/Cu mesh, the photocurrent density and photostability of the graphene modified 1D Cu_2O (G-1.0/Cu_2O/Cu mesh) had been improved by up to 2 and 5 times respectively. In particular, the photocurrents obtained at higher positive bias (0.2−0.4 V vs RHE) from the water reduction potential are the highest reported to date for Cu_2O based photocathode. The enhanced PEC performance is due to the synergistic interaction of graphene towards light absorption together with 1D Cu_2O and is being an excellent electron collector and transporter to separate photogenerated electron-hole pairs. Additionally, the work demonstrates that graphene is suitable for resolving the photocorrosion problem of unstable semiconductors.

Acknowledgment

The financial supports from the Ministry of Science and Technology (MoST(103-3113-E-011 -001, 101-3113-E-011-002, 101-2923-E-011-001-MY3, 100-2221-E-011-105-MY3), the Ministry of Economic Affairs (MOEA) (101-EC-17-A-08-S1-183), and the Top University Projects of Ministry of Education (MOE) (100H451401), as well as the facilities supports from the National Synchrotron Radiation Research Center (NSRRC) and National Taiwan University of Science and Technology (NTUST) are acknowledge

References:

1. N. S. Lewis and D. G. Nocera, *Proceedings of the National Academy of Sciences*, 2006, **103**, 15729-15735.
2. A. FUJISHIMA and K. HONDA, *Nature*, 1972, **238**, 37-38.
3. M. G. Walter, E. L. Warren, J. R. McKone, S. W. Boettcher, Q. Mi, E. A. Santori and N. S. Lewis, in *Chemical Reviews*, American Chemical Society, 2010, pp. 6446-6473.
4. U. Eberle, B. Muller and R. von Helmolt, *Energy & Environmental Science*, 2012, **5**, 8780-8798.
5. J. A. Turner, *Science*, 1999, **285**, 687-689.
6. O. Khaselev and J. A. Turner, *Science*, 1998, **280**, 425-427.
7. S. Xu, J. Ng, A. J. Du, J. Liu and D. D. Sun, *International Journal of Hydrogen Energy*, 2011, **36**, 6538-6545.
8. K. Sivula, F. L. Formal and M. Grätzel, *Chemistry of Materials*, 2009, **21**, 2862-2867.
9. S. Xu, A. J. Du, J. Liu, J. Ng and D. D. Sun, *International Journal of Hydrogen Energy*, 2011, **36**, 6560-6568.
10. M. Li, L. Zhao and L. Guo, *International Journal of Hydrogen Energy*, 2010, **35**, 7127-7133.
11. X.-Y. Zhang, H.-P. Li, X.-L. Cui and Y. Lin, *Journal of Materials Chemistry*, 2010, **20**, 2801-2806.
12. A. Paracchino, J. C. Brauer, J.-E. Moser, E. Thimsen and M. Graetzel, *The Journal of Physical Chemistry C*, 2012, **116**, 7341-7350.
13. A. Paracchino, V. Laporte, K. Sivula, M. GrÃ¤tzel and E. Thimsen, *Nat Mater*, 2011, **10**, 456-461.
14. P. E. de Jongh, D. Vanmaekelbergh and J. J. Kelly, *Journal of The Electrochemical Society*, 2000, **147**, 486-489.
15. C.-Y. Lin, Y.-H. Lai, D. Mersch and E. Reisner, *Chemical Science*, 2012, **3**, 3482-3487.
16. J.-N. Nian, C.-C. Hu and H. Teng, *International Journal of Hydrogen Energy*, 2008, **33**, 2897-2903.
17. Q. Li, P. Xu, B. Zhang, H. Tsai, S. Zheng, G. Wu and H.-L. Wang, *The Journal of Physical Chemistry C*, 2013, **117**, 13872-13878.
18. C. W. Li and M. W. Kanan, *Journal of the American Chemical Society*, 2012, **134**, 7231-7234.
19. Y. H. Lee, I. C. Leu, C. L. Liao, S. T. Chang, M. T. Wu, J. H. Yen and K. Z. Fung, *Electrochemical and Solid-State Letters*, 2006, **9**, A207-A210.
20. J. Cui and U. J. Gibson, *The Journal of Physical Chemistry C*, 2010, **114**, 6408-6412.
21. S. Hacialioglu, F. Meng and S. Jin, *Chemical Communications*, 2012, **48**, 1174-1176.
22. S. N. Baker and G. A. Baker, *Angewandte Chemie International Edition*, 2010, **49**, 6726-6744.
23. A. K. Geim, *Science*, 2009, **324**, 1530-1534.
24. Y. Ahn, Y. Jeong and Y. Lee, *ACS Applied Materials & Interfaces*, 2012, **4**, 6410-6414.
25. R. Tenne, *Nat Nano*, 2006, **1**, 103-111.
26. S.-H. Cheng, T.-M. Weng, M.-L. Lu, W.-C. Tan, J.-Y. Chen and Y.-F. Chen, *Sci. Rep.*, 2013, **3**.
27. M. J. Allen, V. C. Tung and R. B. Kaner, *Chemical Reviews*, 2009, **110**, 132-145.
28. M. Topsakal, H. Şahin and S. Ciraci, *Physical Review B*, 2012, **85**, 155445.
29. Q. Xiang, J. Yu and M. Jaroniec, *Chemical Society Reviews*, 2012, **41**, 782-796.
30. X.-J. Lv, W.-F. Fu, H.-X. Chang, H. Zhang, J.-S. Cheng, G.-J. Zhang, Y. Song, C.-Y. Hu and J.-H. Li, *Journal of Materials Chemistry*, 2012, **22**, 1539-1546.
31. P. D. Tran, S. K. Batabyal, S. S. Pramana, J. Barber, L. H. Wong and S. C. J. Loo, *Nanoscale*, 2012, **4**, 3875-3878.
32. B. Li, T. Liu, L. Hu and Y. Wang, *Journal of Physics and Chemistry of Solids*, 2013, **74**, 635-640.
33. Y. Z. Bo Shen, Qi An, Li Yu, Jiwu Shang, *Desalination and Water Treatment*, 2013.
34. N. Zhigang, *Materials Science in Semiconductor Processing*, 2014, **23**, 78-84.

35. X. Zhang, X. Lu, Y. Shen, J. Han, L. Yuan, L. Gong, Z. Xu, X. Bai, M. Wei, Y. Tong, Y. Gao, J. Chen, J. Zhou and Z. L. Wang, *Chemical Communications*, 2011, **47**, 5804-5806.
36. J. Liu, L. Liu, H. Bai, Y. Wang and D. D. Sun, *Applied Catalysis B: Environmental*, 2011, **106**, 76-82.
37. S. D. Tilley, M. Schreier, J. Azevedo, M. Stefik and M. Graetzel, *Advanced Functional Materials*, 2013, n/a-n/a.
38. Z. Zhang and P. Wang, *Journal of Materials Chemistry*, 2012, **22**, 2456-2464.
39. Z. Zhang, R. Dua, L. Zhang, H. Zhu, H. Zhang and P. Wang, *ACS Nano*, 2013, **7**, 1709-1717.
40. W. S. Hummers and R. E. Offeman, *Journal of the American Chemical Society*, 1958, **80**, 1339-1339.
41. D.-D. La, T. A. Nguyen, S. Lee, J. W. Kim and Y. S. Kim, *Applied Surface Science*, 2011, **257**, 5705-5710.
42. X. An, J. C. Yu, Y. Wang, Y. Hu, X. Yu and G. Zhang, *Journal of Materials Chemistry*, 2012, **22**, 8525-8531.
43. W. Zhang, X. Wen, S. Yang, Y. Berta and Z. L. Wang, *Advanced Materials*, 2003, **15**, 822-825.
44. C. Lu, L. Qi, J. Yang, D. Zhang, N. Wu and J. Ma, *The Journal of Physical Chemistry B*, 2004, **108**, 17825-17831.
45. W. Chen, L. Yan and P. R. Bangal, *Carbon*, 2010, **48**, 1146-1152.
46. A. K. Agegnehu, C.-J. Pan, J. Rick, J.-F. Lee, W.-N. Su and B.-J. Hwang, *Journal of Materials Chemistry*, 2012, **22**, 13849-13854.
47. O. Akhavan, M. Abdolahad, A. Esfandiar and M. Mohatashamifar, *The Journal of Physical Chemistry C*, 2010, **114**, 12955-12959.
48. Y. Mao, J. He, X. Sun, W. Li, X. Lu, J. Gan, Z. Liu, L. Gong, J. Chen, P. Liu and Y. Tong, *Electrochimica Acta*, 2012, **62**, 1-7.
49. D. Powell, A. Compaan, J. R. Macdonald and R. A. Forman, *Physical Review B*, 1975, **12**, 20-25.
50. Z. Wang, V. Pischedda, S. K. Saxena and P. Lazor, *Solid State Communications*, 2002, **121**, 275-279.
51. J. Guo, Y. Li, S. Zhu, Z. Chen, Q. Liu, D. Zhang, W.-J. Moon and D.-M. Song, *RSC Advances*, 2012, **2**, 1356-1363.
52. H. Huang, Z. Yue, G. Li, X. Wang, J. Huang, Y. Du and P. Yang, *Journal of Materials Chemistry A*, 2013, **1**, 15110-15116.
53. J.-H. Zhong, G.-R. Li, Z.-L. Wang, Y.-N. Ou and Y.-X. Tong, *Inorganic Chemistry*, 2010, **50**, 757-763.
54. L. Jia, D.-H. Wang, Y.-X. Huang, A.-W. Xu and H.-Q. Yu, *The Journal of Physical Chemistry C*, 2011, **115**, 11466-11473.
55. Q. Li, B. Guo, J. Yu, J. Ran, B. Zhang, H. Yan and J. R. Gong, *Journal of the American Chemical Society*, 2011, **133**, 10878-10884.
56. W. Zhao, W. Fu, H. Yang, C. Tian, M. Li, Y. Li, L. Zhang, Y. Sui, X. Zhou, H. Chen and G. Zou, *CrystEngComm*, 2011, **13**, 2871-2877.
57. Y. Lin, C. Battaglia, M. Boccard, M. Hettick, Z. Yu, C. Ballif, J. W. Ager and A. Javey, *Nano Letters*, 2013, **13**, 5615-5618.
58. I. V. Lightcap, T. H. Kosel and P. V. Kamat, *Nano Letters*, 2010, **10**, 577-583.
59. Y. H. Ng, A. Iwase, A. Kudo and R. Amal, *The Journal of Physical Chemistry Letters*, 2010, **1**, 2607-2612.
60. Y. Li, T. Takata, D. Cha, K. Takanabe, T. Minegishi, J. Kubota and K. Domen, *Advanced Materials*, 2013, **25**, 125-131.
61. A. Paracchino, N. Mathews, T. Hisatomi, M. Stefik, S. D. Tilley and M. Gratzel, *Energy & Environmental Science*, 2012, **5**, 8673-8681.
62. Y. Hou, F. Zuo, A. Dagg and P. Feng, *Nano Letters*, 2012, **12**, 6464-6473.
63. C. Liu, Y. Teng, R. Liu, S. Luo, Y. Tang, L. Chen and Q. Cai, *Carbon*, 2011, **49**, 5312-5320.

64. C. G. Morales-Guio, S. D. Tilley, H. Vrubel, M. Gratzel and X. Hu, *Nat Commun*, 2014/01/08/**5**.
65. E. S. Kim, N. Nishimura, G. Magesh, J. Y. Kim, J.-W. Jang, H. Jun, J. Kubota, K. Domen and J. S. Lee, *Journal of the American Chemical Society*, 2013, **135**, 5375-5383.
66. X. Zhang, Y. Liu, S.-T. Lee, S. Yang and Z. Kang, *Energy & Environmental Science*, 2014, **7**, 1409-1419.
67. A. Gaur and B. D. Shrivastava, *ACTA PHYSICA POLONICA A*, 2012, **121**, 647-652.
68. S. Bijani, M. Gabas, G. Subias, J. Garcia, L. Sanchez, J. Morales, L. Martinez and J. R. Ramos-Barrado, *Journal of Materials Chemistry*, 2011, **21**, 5368-5377.
69. Z. Chen, T. F. Jaramillo, T. G. Deutsch, A. Kleiman-Shwarsctein, A. J. Forman, N. Gaillard, R. Garland, K. Takanabe, C. Heske, M. Sunkara, E. W. McFarland, K. Domen, E. L. Miller, J. A. Turner and H. N. Dinh, *Journal of Materials Research*, 2010, **25**, 3-16.
70. Q. Huang, F. Kang, H. Liu, Q. Li and X. Xiao, *Journal of Materials Chemistry A*, 2013, **1**, 2418-2425.
71. E. C. Heltemes, *Physical Review*, 1966, **141**, 803-805.
72. L. C. Wang, N. R. de Tacconi, C. R. Chenthamarakshan, K. Rajeshwar and M. Tao, *Thin Solid Films*, 2007, **515**, 3090-3095.
73. Y.-K. Hsu, C.-H. Yu, Y.-C. Chen and Y.-G. Lin, *Electrochimica Acta*, 2013, **105**, 62-68.
74. J. Gu, A. Wuttig, J. W. Krizan, Y. Hu, Z. M. Detweiler, R. J. Cava and A. B. Bocarsly, *The Journal of Physical Chemistry C*, 2013, **117**, 12415-12422.